ARTICLE OPEN

Check for updates

The role of extracellular polymeric substances of fungal biofilms in mineral attachment and weathering

Romy Breitenbach[1,7], Ruben Gerrits[1,7], Polina Dementyeva[1], Nicole Knabe[1], Julia Schumacher[1,2], Ines Feldmann[1], Jörg Radnik[3], Masahiro Ryo[4,5] and Anna A. Gorbushina[1,2,6]✉

The roles extracellular polymeric substances (EPS) play in mineral attachment and weathering were studied using genetically modified biofilms of the rock-inhabiting fungus *Knufia petricola* strain A95. Mutants deficient in melanin and/or carotenoid synthesis were grown as air-exposed biofilms. Extracted EPS were quantified and characterised using a combination of analytical techniques. The absence of melanin affected the quantity and composition of the produced EPS: mutants no longer able to form melanin synthesised more EPS containing fewer pullulan-related glycosidic linkages. Moreover, the melanin-producing strains attached more strongly to the mineral olivine and dissolved it at a higher rate. We hypothesise that the pullulan-related linkages, with their known adhesion functionality, enable fungal attachment and weathering. The released phenolic intermediates of melanin synthesis in the Δ*sdh1* mutant might play a role similar to Fe-chelating siderophores, driving olivine dissolution even further. These data demonstrate the need for careful compositional and quantitative analyses of biofilm-created microenvironments.

npj Materials Degradation (2022)6:42 ; https://doi.org/10.1038/s41529-022-00253-1

INTRODUCTION

Fungi-mineral interactions take place from the lithosphere-atmosphere border[1] to the deep subsurface of our planet[2], but their influence on biogeochemical processes is especially significant in aerobic terrestrial environments[3]. In these vast niches, fungi acquire nutrients via the breakdown of airborne dust and (soil) organic matter, the allocation of carbon from phototrophic symbionts, and the weathering of rock substrates[4–6].

Significance of fungal studies in biogeochemistry and geobiology is rooted in the fact that fungi are active in mineral weathering and biofilm formation. Microbial biofilms play key roles within the biosphere as the primary colonisers of new habitats, and as contributors of biomass and energy at the base of food webs[7]. However, so far research of fungal biofilms belongs mainly to the realm of medical mycology, and it is time to change this perception.

To mechanistically study fungi-mineral interactions, we singled out black environmental rock-inhabiting fungi—ubiquitous and dominant settlers on sun- and air-exposed mineral surfaces[8,9]. Under the impact of various stresses like solar radiation, desiccation, de/re-hydration, temperature fluctuations, and lack of nutrients[10] these microbial biofilms contribute to weathering and soil formation[11]. Known for their ability to form visible and biodeteriorating biofilms on exposed desert rocks and anthropogenic substrates like solar panels[12,13], rock-inhabiting fungi are relevant to the study of material sciences and geo(micro)biology[14].

These fungi produce EPS[15] and are black as they produce the dark DHN (1,8-dihydroxynaphthalene) melanin[16]. This pigment is common in several Ascomycetes and accumulates in the walls of yeast- and hyphae-like cells, sexual and asexual spores, as well as in resting and reproduction structures of different species. The synthesis pathway can roughly be divided into three steps, namely the *de novo* synthesis of the phenolic pentaketide T4HN (1, 3, 6, 8 tetrahydroxynaphthalene), its modification to DHN, and the oxidative polymerisation of DHN resulting in the highly complex DHN melanin[17]. Slightly different routes for the synthesis of DHN exist; however, all synthetic pathways include T4HN as an intermediate which is converted via scytalone, T3HN (1,3,8-trihydroxynaphthalene) and vermelone to DHN by highly conserved enzymes: T4HN/T3HN reductases and scytalone reductase (SDH). Elimination of enzymes catalysing the later steps in the pathway results in the accumulation of coloured intermediates and shunt products, but the deletion of the key enzyme (polyketide synthase, PKS)-encoding gene prevents the formation of any melanin precursors[18,19].

EPS and melanin form the outer interactive layers of all black fungi and have similar functions. Melanin can protect the organism from extreme temperatures[20,21], metal toxicity[22], osmotic stress, and desiccation[23,24]. Diverse EPS components—extracellular proteins, lipids, polysaccharides, and DNA—all lend stability to the biofilm by mediating cellular aggregation and brings the cells in a close contact to the substrate by enabling adhesion[7]. Proteins and polysaccharides specifically protect biofilms from desiccation through the retention of water, serve as a barrier against antimicrobial substances and toxic metals, accumulate nutrients from the environment, and embed extracellular enzymes, and metabolites, ensuring their stability[7]. Though the above-listed protective properties of cell-surrounding outer layers are known, the role of EPS in weathering is not yet firmly established and ambiguous. EPS may enhance the weathering of silicates by itself but block the weathering action of other metabolites[25]

[1]Abteilung 4, Material und Umwelt, Bundesanstalt für Materialforschung und -prüfung (BAM), 12205 Berlin, Germany. [2]Fachbereich Biologie, Chemie und Pharmazie, Freie Universität Berlin, 14195 Berlin, Germany. [3]Abteilung 6, Materialchemie, Bundesanstalt für Materialforschung und -prüfung (BAM), 12205 Berlin, Germany. [4]Artificial Intelligence for Smart Agriculture, Leibniz Centre for Agricultural Landscape Research (ZALF), 15374 Müncheberg, Germany. [5]Brandenburg University of Technology Cottbus–Senftenberg, 03046 Cottbus, Germany. [6]Fachbereich Geowissenschaften, Freie Universität Berlin, 12249 Berlin, Germany. [7]These authors contributed equally: Romy Breitenbach, Ruben Gerrits. ✉email: anna.gorbushina@bam.de

In this study, we examined the EPS and determined the olivine dissolution rate of several pigment mutants of *K. petricola*: Δ*pks1*, which no longer is able to produce any melanin intermediate, Δ*sdh1* which cannot produce melanin but still the intermediate scytalone, Δ*phd1* which no longer can produce carotenoids but still the colourless carotenoid-intermediate phytoene, and Δ*pks1*/Δ*phd1* which can neither produce melanin nor coloured carotenoids[18]. For EPS studies, fungi were cultivated as subaerial biofilms and the EPS matrix was characterised by weight, general chemistry, glycosidic linkages, and monosaccharide composition using gas chromatography-mass spectrometry (GC-MS), X-ray photoelectron spectroscopy (XPS), and Fourier transform infrared spectroscopy (FTIR). Fungal cell wall and EPS layers were visualised by cryo-scanning electron microscopy (cryo-SEM), transmission electron microscopy (TEM), and confocal laser scanning microscopy (CLSM). Batch olivine dissolution experiments served to determine the ability of each strain to dissolve olivine. Mg, Si, and Fe concentrations were analysed by inductively coupled plasma optical emission spectroscopy (ICP-OES): the time-series of the aqueous Mg concentrations provided olivine dissolution rates. The growth behaviour of each strain in the reactors was analysed using a dissecting microscope and SEM.

RESULTS

Biofilm and EPS morphology

The *K. petricola* wild type (WT) and the carotenoid-deficient mutant Δ*phd1* grew a thicker biofilm than the Δ*pks1* and Δ*pks1*/Δ*phd1* melanin-deficient mutants, which build biofilms of a predominantly flat structure, only slightly corrugated at the edges (Fig. 1). The orange-brown mutant Δ*sdh1*, which accumulates DHN melanin precursors, grew a biofilm with a thickness in between that of the biofilm of the WT and the Δ*pks1* mutant.

As expected, TEM imaging revealed that only the melanin-producing strains (i.e., the WT and Δ*phd1* mutant) formed a continuous layer of melanin in the cell wall (Fig. 1). The melanin-deficient mutants Δ*pks1* and Δ*pks1*/Δ*phd1* did not form this layer. The mutant Δ*sdh1*, which produces orange-brown melanin precursors, formed a cell wall which is not completely pigmented: it is interrupted at several positions (Fig. 1). An EPS layer could be visualised around the cells of all strains by cryo-SEM and TEM. This layer was however more distinct in melanin-lacking biofilms formed by Δ*pks1*, Δ*pks1*/Δ*phd1,* and Δ*sdh1*.

EPS quantification

This microscopic analysis was confirmed by EPS extraction and quantification (Fig. 2). The mutant Δ*phd1* produced 107 ± 23 mg EPS g^{-1} biomass and thus showed no significant difference to the EPS amount produced by the WT (102.9 ± 5.0 mg g^{-1})[15]. In contrast, EPS production by the melanin-deficient mutant Δ*pks1* (189 ± 45 mg g^{-1}) was significantly ($p < 0.05$, $n = 3$) higher than by the WT. The Δ*sdh1* and Δ*pks1*/Δ*phd1* mutants produced 136 ± 33 and 188 ± 75 mg g^{-1}, respectively, not significantly ($p > 0.05$, $n = 3$) more than the WT.

Lectin screening

The fluorescence lectin barcoding was performed with lectins from an existing library[26], to test their binding capacities to glycoconjugates of *K. petricola* WT and Δ*pks1*/Δ*phd1* biofilms. 12 and 26 lectins tested bound to the EPS of the WT and the mutant Δ*pks1*/Δ*phd1*, respectively (Supplementary Table 3). Of these, 16 lectins bound exclusively to glycoconjugates of the melanin- and carotenoid-lacking mutant. In addition, the two lectins NPA and PMA only bound for the WT biofilms. Lectins with potentially interesting binding patterns were selected for a more detailed fluorescence lectin binding analysis. In addition to the WT and the Δ*pks1*/Δ*phd1* mutant, the Δ*pks1* mutant was included in this analysis. Supplementary Figure 1 shows an example of the bonding pattern of two of these lectins: HHA and GNA. HHA, which is known to have a binding specificity for α-mannose units in glycoconjugates[26], a unit that can also be found in the EPS of *K. petricola*[15], showed a good EPS binding. This is even more the case for the melanin-deficient mutants: due to its reduced diffusion through the WT biofilms, the inner sections of these biofilms did not give a signal. The partial labelling of the WT biofilms was also observed for other lectins (data not shown). In addition, for most lectins, no clear distinction could be made between the binding of EPS and cell wall. Particularly in the WT, the EPS is tightly bound to the cells, making it difficult to distinguish between the EPS and the cell wall. However, with the lectin GNA, which has also a binding specificity for α-mannose units[26], double rings were repeatedly observed, with the inner ring probably showing the cell wall and the outer ring the EPS layer (Supplementary Fig. 1).

Spectroscopical EPS analysis by XPS and FTIR

The atomic ratios and the functional groups of the EPS of all strains were analysed by XPS (Supplementary Table 4) and FTIR (Supplementary Fig. 2), respectively. XPS analyses of the outermost cell surface layers revealed similar O/C and N/C ratios for all strains, except for Δ*sdh1*: the EPS of this mutant had a higher N/C ratio compared to the other strains.

The FTIR spectra of the EPS of the pigment mutants (Supplementary Fig. 2) agree with the previous analysis of the WT EPS[15]. The broad band around 3305–3262 cm^{-1} can represent the stretching vibration of the N–H bonds of amides or amines or the H-bond of O–H groups[27]. This band was much stronger for the Δ*sdh1* mutant than for the other strains. The weak absorption band at 2936–2888 cm^{-1} is related to C–H stretching of CH_3- or CH_2-groups, while bands at 1661–1552 cm^{-1} can be assigned to C=O stretching and N–H bending of amide groups[27]. These latter bands were weaker for the WT than for the pigment mutants. The characteristic carbohydrate bands at 1440–1350 cm^{-1} likely represent C–H deformations, O–H bending, or the stretching of C–O bonds of carboxyl groups[27]. The maximum for the WT EPS was at 1429 cm^{-1}, whereas for the EPS of all pigment mutants this maximum shifted to 1375 ± 2 cm^{-1}. The bands at 1021, 1029, 1075, 1080, and 1082 cm^{-1} for the EPS of WT, Δ*phd1*, Δ*pks1*, Δ*pks1*/Δ*phd1,* and Δ*sdh1*, respectively represent C–O stretching vibrations of alcohol, ether or carboxyl groups[27]. Polysaccharides show specific band maxima in the range 1200–1000 cm^{-1} depending on the monosaccharide composition[28]. Cerna et al.[29] specified the range 1100–1030 cm^{-1} with a maximum at 1068 cm^{-1} for galactose, maxima at 1072 and 1033 cm^{-1} for mannose, and maximuma within a range of 1030–944 cm^{-1} for glucose. The maxima for the WT and the Δ*phd1* mutant's EPS were at 1021 and 1029 cm^{-1}, respectively (Supplementary Fig. 2), indicating that the main portion of their extracellular polysaccharides is glucose. The observed shifts for the EPS of the melanin mutants to 1075 cm^{-1} for Δ*pks1*, 1080 cm^{-1} for Δ*pks1*/Δ*phd1,* and 1082 cm^{-1} for Δ*sdh1* suggest that the amount of mannose and galactose was elevated in their extracellular polysaccharides.

Polysaccharide composition of the EPS

As shown for the WT[15], the exopolysaccharides of all pigment mutants are composed of the three hexoses mannose (21 ± 11%), glucose (66.3 ± 5.4%), and galactose (12.3 ± 5.8%) (Fig. 2b). Compared to the EPS of the WT, the EPS of the Δ*phd1* mutant had a similar composition of mannose (25 ± 14%), glucose (60 ± 15 %), and galactose (14.72 ± 0.74%). The exopolysaccharides of the Δ*pks1*, Δ*pks1*/Δ*phd1*, and Δ*sdh1* mutants had a monosaccharide composition deviating from the WT; glucose was still the monosaccharide with the highest proportion (41.9 ± 5.7%, 41%,

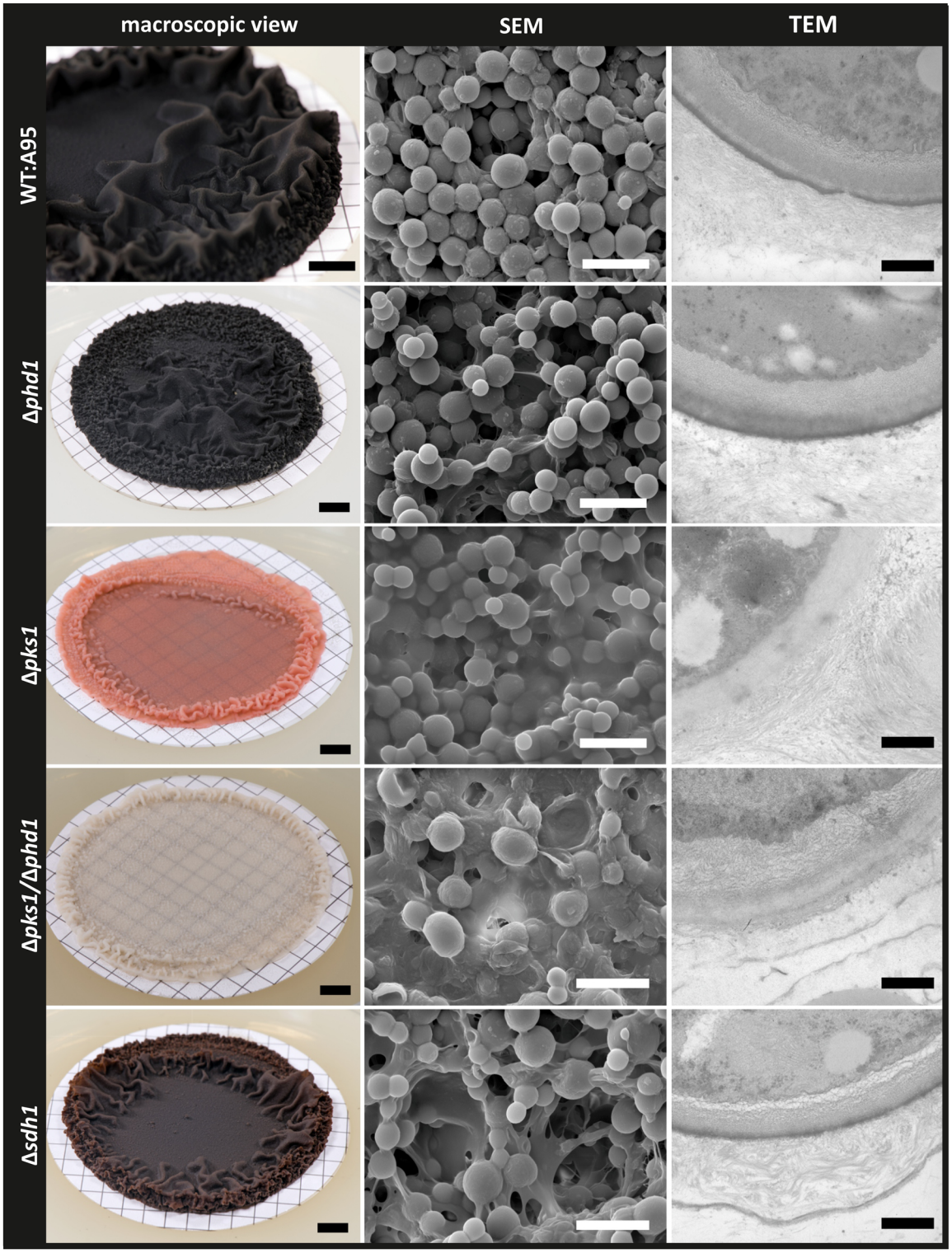

Fig. 1 Imaging of *K. petricola* WT and pigment mutant biofilms. Macroscopic photographs show the morphology of the fungal biofilms. Cryo-scanning electron microscopy (cryo-SEM) and transmission electron microscopy (TEM) imaging show a close-up view of the biofilms and cell walls with EPS of single cells. Scale bar in macroscopic photographs = 5 mm; in SEM pictures = 20 µm and in TEM pictures = 500 nm.

and 38.9 ± 8.2%, respectively), however, the amount of mannose (31 ± 12%, 32%, and 36.8 ± 2.6%) and galactose (26.9 ± 6.5%, 27%, and 24.3 ± 5.6%) was higher.

All glycosidic linkages from the WT exopolysaccharides described in Breitenbach et al.[15], could also be detected for the pigment mutants (Table 1 for the average values) and qualitative differences can be excluded. In part, however, the glycosidic linkages showed significant quantitative deviations. As with the results of the FTIR and monosaccharide analyses, the relative amounts of the glycosidic linkages of the Δ*phd1* mutant did not differ significantly from those of the WT. Quantitative differences could be observed for the melanin-free mutants Δ*pks1* and Δ*pks1*/

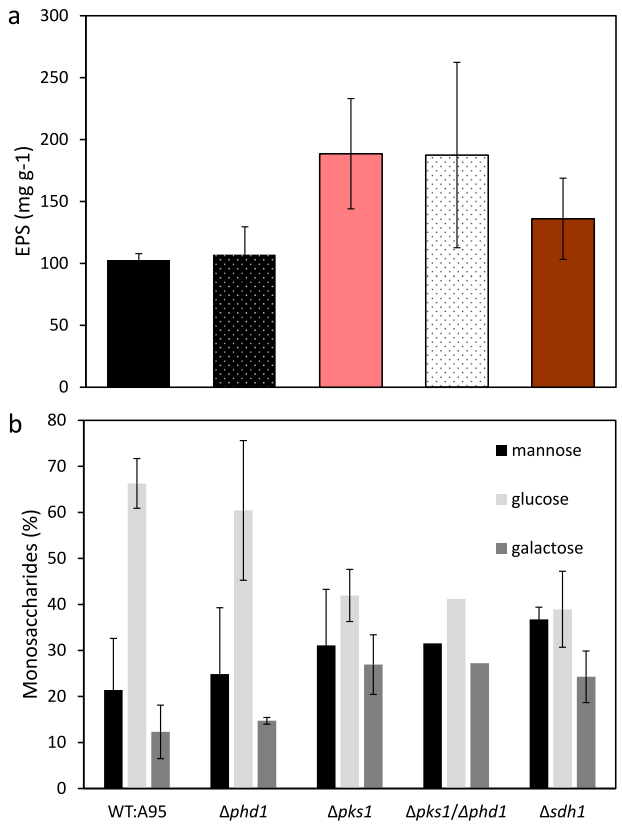

Fig. 2 EPS amounts and monosaccharide compositions of biofilms of *K. petricola* WT and pigment mutants. Shown are the averages together with two times the standard error of the biological replicates (except for the monosaccharide composition of Δ*pks1*/Δ*phd1*, for which one biological replicate was analysed and no uncertainty is given). The WT data have already been published[15] and are shown here again for comparison with the mutant strains. **a** The amounts of EPS produced by *K. petricola* WT and Δ*phd1* are lower than the EPS amounts produced by the Δ*pks1* and Δ*pks1*/Δ*phd1* mutant strains. **b** The monosaccharide compositions of *K. petricola* WT and Δ*phd1* are different from the composition of the other pigment mutant strains.

Δ*phd1*: even though the ratio of the linkages (1 → 4)-Glc*p* to (1 → 6)-Glc*p* was approximately 2:1 (as it was for the WT), the relative amount of both linkages decreased significantly ($p < 0.05$, $n = 3$) compared to the WT. The glycosidic linkage (1 → 3,6)-Glc*p* in the Δ*pks1* mutant was present in a significantly ($p < 0.05$, $n = 3$) higher amount compared to the WT. Moreover, for both the Δ*pks1* and Δ*pks1*/Δ*phd1* mutants the relative amount of terminal connections (1 →)-Glc*p*, (1 →)-Man*p* and (1 →)-Gal*f* and the linkages (1 → 2)-Man*p*, (1 → 3)-Glc*p* and (1 → 6)-Gal*f* was higher than for the WT. The linkage pattern of the Δ*sdh1* mutant ranged between the WT and the melanin-lacking mutant Δ*pks1*.

Fungal biofilm effect on olivine dissolution

All tested strains were able to grow in the olivine dissolution reactors without any significant ($p > 0.05$, $n = 3$) differences in final biomass (Supplementary Table 5 and Supplementary Fig. 3). The colour of the liquid medium of the Δ*sdh1* set-up changed to orange-brown (data not shown). The pH in all set-ups remained around 6 over the course of the experiment as the used medium solution was pH-buffered (Fig. 3a). The set-ups with Δ*pks1* (5.90 ± 0.02) and Δ*pks1*/Δ*phd1* (5.90 ± 0.02) had a significantly ($p < 0.01$, $n = 3$) lower final pH than those with the WT (5.99 ± 0.03), Δ*phd1* mutant (5.97 ± 0.04), Δ*sdh1* mutant (6.02 ± 0.02) and the abiotic set-ups (6.02 ± 0.04).

Overall, the release of Mg and Si in the dissolution experiments was stoichiometric (Fig. 3e). Mg and Si aqueous concentrations were lowest ($p < 0.01$, $n = 3$) in the abiotic set-up, followed by Δ*pks1* and Δ*pks1*/Δ*phd1* set-ups, and the WT and Δ*phd1* set-ups. Both concentrations were highest for the Δ*sdh1* set-up (all differences significant, $p < 0.01$, $n = 3$) (Fig. 3b, c).

The Fe concentrations of the Δ*sdh1*, Δ*pks1*, and Δ*pks1*/Δ*phd1* set-ups were significantly ($p < 0.01$, $n = 3$) higher than of the abiotic, WT, and Δ*phd1* set-ups (Fig. 3d). The release of Fe in all experimental set-ups was far from stoichiometric (Fig. 3f): Fe/Si ratios of the Δ*sdh1*, Δ*pks1*, and Δ*pks1*/Δ*phd1* set-ups were again significantly ($p < 0.05$, $n = 3$) higher than those of the abiotic, WT and Δ*phd1* set-ups (Fig. 3f).

The abiotic olivine dissolution rate at day 55 ($9.7 \pm 4.1 \times 10^{-16}$ mol cm^{-2} s^{-1}) was lower ($p < 0.01$, $n = 3$) than all biotic dissolution rates (Fig. 4a and Supplementary Table 5). The WT ($38 \pm 13 \times 10^{-16}$ mol cm^{-2} s^{-1}) and Δ*phd1* mutant ($34 \pm 12 \times 10^{-16}$ mol cm^{-2} s^{-1}) had higher ($p < 0.01$, $n = 3$) olivine dissolution rates compared to

Table 1. Glycosidic linkages derived from the partially O-methylated alditol acetates obtained by methylation analyses of *K. petricola* EPS.

Permethylated alditol acetate	Mol %					
	WT:A95	Δ*phd1*	Δ*pks1*	Δ*pks1*/Δ*phd1*	Δ*sdh1*	Glycosidic linkage
2,3,4,6-Me_4-Glc*p*	7.8	5.9	9.0	11.4	8.5	Glc*p*-(1→
2,3,4,6-Me_4-Man*p*	1.6	*tr*	7.1	5.1	3.7	Man*p*-(1→
2,3,5,6-Me_4-Gal*f*	4.1	2.5	9.9	10.0	4.5	Gal*f*-(1→
3,4,6-Me_3-Man*p*	2.0	1.6	7.9	8.8	1.7	2→)-Man*p*-(1→
2,4,6-Me_3-Glc*p*	*tr*	*tr*	7.3	6.5	1.7	3→)-Glc*p*-(1→
2,3,6-Me_3-Glc*p*	50.7	51.0	20.4	25.1	45.8	4→)-Glc*p*-(1→
2,3,4-Me_3-Glc*p*	22.1	30.5	14.5	10.1	19.0	6→)-Glc*p*-(1→
2,3,5-Me_3-Gal*f*	2.6	1.7	13.0	9.1	4.8	6→)-Gal*f*-(1→
2,6-Me_2-Glc*p*	4.7	4.3	2.7	8.7	8.0	3,4→)-Glc*p*-(1→
2,4-Me_2-Glc*p*	4.4	2.5	8.2	5.2	2.3	3,6→)-Glc*p*-(1→

Man, mannose; Glc, Glucose, Gal, Galactose; *f*, furanose form; *p*, pyranose form; tr, traces. The WT data have already been published[15] and are shown again for comparison. The mean values of three biological replicates are listed. The uncertainty representing twice the standard error of the biological replicates is given in the supplementary data file.

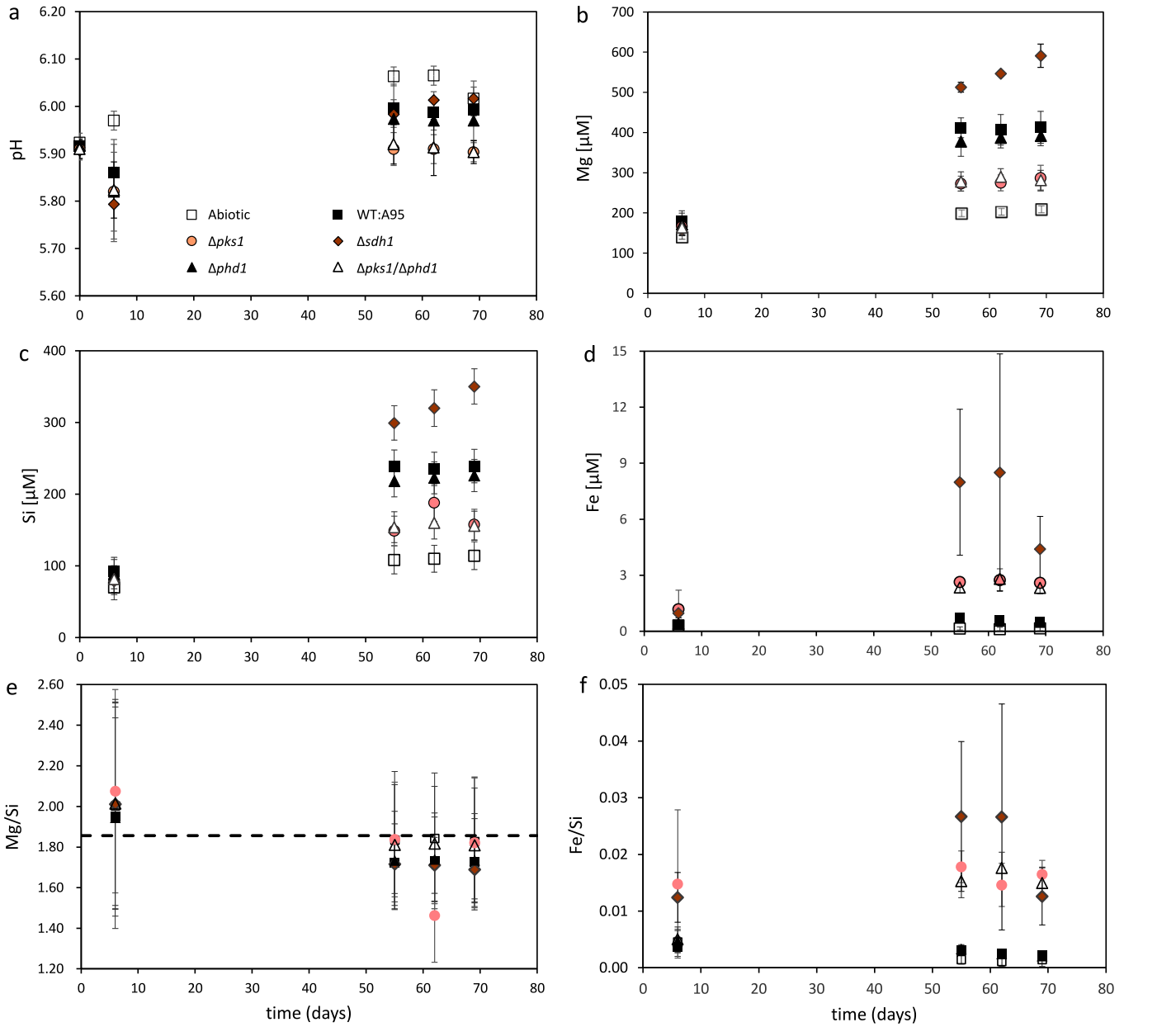

Fig. 3 Temporal evolution of the pH and Mg (µM), Si (µM), and Fe (µM) concentration and the Mg/Si and Fe/Si concentration ratios of the olivine dissolution experiments. a The pH remained stable during the experiment and was slightly lower for the melanin-deficient Δ*pks1* and Δ*pks1*/Δ*phd1* mutants at the end of the experiment. **b**, **c** The Mg and Si concentrations (µM) increased during the experiment and were highest for the Δ*sdh1* mutant. **d** The Fe concentration (µM) increased for the Δ*sdh1*, Δ*pks1*, and Δ*pks1*/Δ*phd1* mutants and was highest for the former. The Fe concentration of the WT, Δ*phd1* mutant, and abiotic control was lower and stayed constant during the experiment. **e** Stoichiometric dissolution is illustrated by the dotted line at Mg/Si = 1.856: all set-ups showed a stoichiometric Mg/Si release. **f** For Fe/Si, stoichiometric dissolution is not shown, lying at Fe/Si = 0.1726. Fe/Si release was far below this ratio for all set-ups, indicating the removal of Fe from the solution. However, the Δ*sdh1*, Δ*pks1*, and Δ*pks1*/Δ*phd1* mutants had significantly higher Fe/Si ratios than the abiotic control, WT, and Δ*phd1* mutant, indicating their ability to keep iron in solution. Error bars represent either twice the analytical uncertainty or twice the standard error of three biological replicates, whichever was highest. For the concentration ratios, they represent twice the combined propagated uncertainties of either Mg and Si (for Mg/Si) or Fe and Si (for Fe/Si). If the error bars are not visible they are smaller than the symbol.

the Δ*pks1* ($17.6 \pm 6.5 \times 10^{-16}$ mol cm^{-2} s^{-1}) and Δ*pks1*/Δ*phd1* ($18.8 \pm 6.9 \times 10^{-16}$ mol cm^{-2} s^{-1}) mutants. The Δ*sdh1* mutant showed the highest ($p < 0.01$, $n = 3$) dissolution rate: $59 \pm 19 \times 10^{-16}$ mol cm^{-2} s^{-1}.

The WT (grade of attachment of 28.7 ± 8.4%) and the mutants Δ*phd1* (47 ± 12%), and Δ*sdh1* (19.3 ± 3.4%) attached more ($p < 0.01$, $n = 3$) to the olivine than the Δ*pks1* (6.8 ± 3.2%) and Δ*pks1*/Δ*phd1* (5.4 ± 2.6%) mutants (Fig. 4c and Supplementary Table 5).

SEM images of olivine-fungus samples taken from the reactors after the olivine dissolution experiments are shown in Supplementary Fig. 4. As expected, no microorganisms were observed on the olivine in the abiotic controls (Supplementary Fig. 4a). Olivine from the biotic experiments was colonised (Supplementary Fig. 4b–f): the WT and Δ*phd1* set-ups showed an enhanced ability to attach to the olivine grains, confirming the reported grades of attachment. EPS was visible around most cells. The thread-like

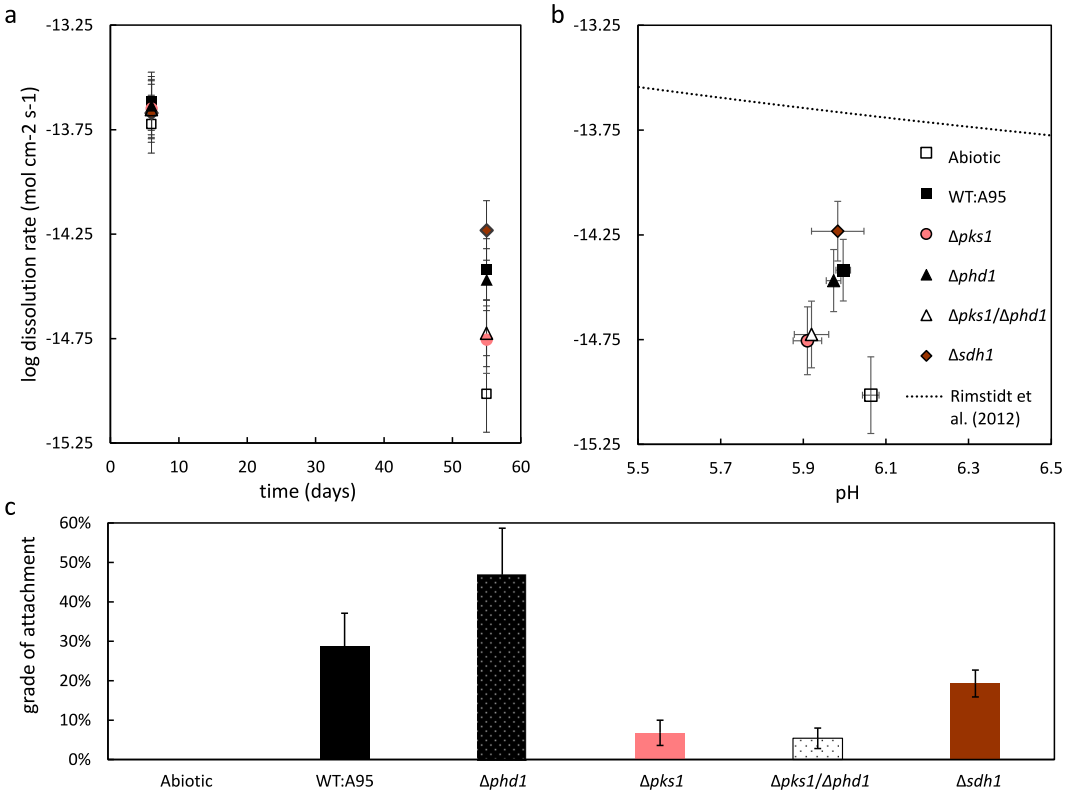

Fig. 4 The dissolution rates as a function of time and pH together with the grades of attachment. a The dissolution rates (mol cm^{-2} s^{-1}) were lower at day 55 than at day 6, indicating that olivine dissolution slows down. **b** The dissolution rates (at day 55) as a function of the pH together with olivine dissolution rate data from the literature (curve calculated using equations reported by Rimstidt et al. (2012)). The dissolution rates from our experiments were lower than those from the literature, again indicating inhibition of dissolution. **c** The grade of attachment (%) to the olivine for the WT (WT:A95) and mutants of *K. petricola* at the end of the experiment (i.e., day 69). Whereas the higher grade of attachment seems to explain the higher olivine dissolution rates for the WT and Δ*phd1* mutant compared to the Δ*pks1* and Δ*pks1*/Δ*phd1* mutants, this is not the case for the Δ*sdh1* mutant. Error bars represent twice the standard error of the three biological replicates or twice the (propagated) analytical uncertainty, whichever was highest.

appearance of the EPS is a preparation artefact (caused by the ethanol dehydration[15]). The chemistry of the mineral precipitates (<1 µm) in the EPS of all strains could not be determined by energy-dispersive X-ray spectroscopy as these were too small.

DISCUSSION

The comparison between the WT and carotenoid- and melanin-deficient mutants allows us to assign functions to the protective outer cell wall envelopes of *K. petricola*. The absence of melanin influences the quantity and composition of the EPS, which in their turn impacts the fungal capacity to attach and dissolve the mineral olivine.

All melanin-deficient mutants possessed elevated amounts of EPS (Fig. 2a), indicating a closer interrelation between EPS and melanin production. Considering EPS' role in protection against dehydration, antimicrobial substances, and toxic metal ions and EPS' ability to accumulate nutrients[30], the higher EPS production of both melanin-deficient mutants might compensate for their melanin deficiency and contribute to stress-tolerance. This assumption is supported by the similar EPS production by the WT and the fully melanised Δ*phd1* mutant (Fig. 2a). The incompletely melanised cell wall of the Δ*sdh1* mutant and its mediocre EPS production (i.e., not significantly ($p > 0.05$, $n = 3$) different from either the melanin-deficient mutants or the WT) also confirms our hypothesis.

The chemical analysis of the EPS by XPS and FTIR correlate. The higher N/C ratio of the *sdh1* mutant detected by XPS (Supplementary Table 4) likely reveals a higher protein content of its surface layers (i.e., its EPS)[31]. This is corroborated by FTIR analysis of this mutant's EPS: the stronger amide-related bands also indicate the presence of proteins (Supplementary Fig. 2). The FTIR bands at 1200–1000 cm^{-1} furthermore showed that the extracellular polysaccharides of the Δ*pks1*, Δ*pks1*/Δ*phd1*, and Δ*sdh1* mutants contained more mannose and galactose and less glucose compared to the WT and Δ*phd1* mutant (Supplementary Fig. 2) agreeing with the analysis of the polysaccharidic composition of the EPS (Fig. 2b).

EPS functions depend on the presence of polysaccharidic polymers[32]. From the analysis of glycoside linkages we deduced the polymeric composition of *K. petricola*'s extracellular polysaccharides. As the relative amount of certain glycosidic linkages was different for Δ*pks1* and Δ*pks1*/Δ*phd1* compared to the WT and Δ*phd1*, but their ratio remained constant (Table 1), we assume that the glycosidic linkages (1 → 4)-Glc*p* and (1 → 6)-Glc*p* and (1 → 2)-Man*p*, (1 → 3)-Glc*p*, and (1 → 6)-Gal*f* are solely related to two polymers, α-glucan and α/β-galactofuromannan, respectively (for details see Breitenbach et al.[15]). The absence of melanin synthesis in Δ*pks1* and Δ*pks1*/Δ*phd1* correlated to a relatively higher amount of the potential galactofuromannan. Both melanin and structural polysaccharides (e.g., galactofuromannan) contribute to the structure and integrity of the cell wall and thus support growth—as well as the cell wall rigidity that have been related to the substrate penetration ability of black fungi[33]. The common role of melanin and galactofuromannan is postulated for fungal virulence (host interaction)[34–37] and fungal growth and cell wall integrity[38–42]. The increased production of galactofuromannan could thus contribute to the structural strength of the cell wall to

cope with the absence of melanin. Polysaccharides and melanin may also be linked/bound in the cell wall[43] and thus reciprocally influence each other's mobility in the cell wall and biofilm matrix.

The higher olivine dissolution rates of the WT and Δ*phd1* mutant compared to the Δ*pks1* and Δ*pks1*/Δ*phd1* mutants (Fig. 4a) correlated both with the presence of melanin and the higher attachment capacities of these mutants. From a previous study, we know of the low olivine dissolution rates of some unattached, melanin-producing WT cultures[44]. Thus, the capacity of *K. petricola* to attach to the mineral surface is a more probable cause of the higher dissolution rates than its melanisation. Interestingly, the grade of attachment correlated to the fraction of α-glucan-related (1 → 4)-Glc*p* and (1 → 6)-Glc*p* linkages of the EPS ($r = 0.94$, 95%CI = [0.35,1.00], $p = 0.017$, Supplementary Table 6). This extracellular polysaccharide, also called pullulan, steers the adhesion capacity of its eponymous fungus *Aureobasidium pullulans*[45,46]. We speculate that also other EPS components of *K. petricola* like proteins and DNA, which were here only marginally studied in the case of protein-rich cell surface of the Δ*sdh1* mutant, might be important for cell attachment[7] and that their composition or quantity could also have been altered upon the deletion of melanin synthesis.

Furthermore, the difference of the Mg concentration of the WT compared to the abiotic control and the Δ*pks1* and Δ*pks1*/Δ*phd1* mutants increased only between day 6 and 55 (Fig. 5), indicating that the effect of attachment on the dissolution rate ended at or before day 55. As the experiment was run in batch, a shortage of nutrients or an accumulation of metabolites might have halted the fungal colonisation of new olivine surface, stopping the effect of attachment.

Attachment is an important bio-mechanical weathering mechanism[3]. In our study, relevant mechanisms related to attachment are the prevention of the dissolution-inhibiting actions of Fe oxidation and the creation of a local acidic or reduced environment near the olivine surface. Abiotic olivine dissolution was inhibited as expressed by decreasing olivine dissolution rates (Fig. 4a) and the final abiotic dissolution rates that were over one order of magnitude lower than those from the literature (as compiled by Rimstidt et al.[47], Fig. 4b, even when

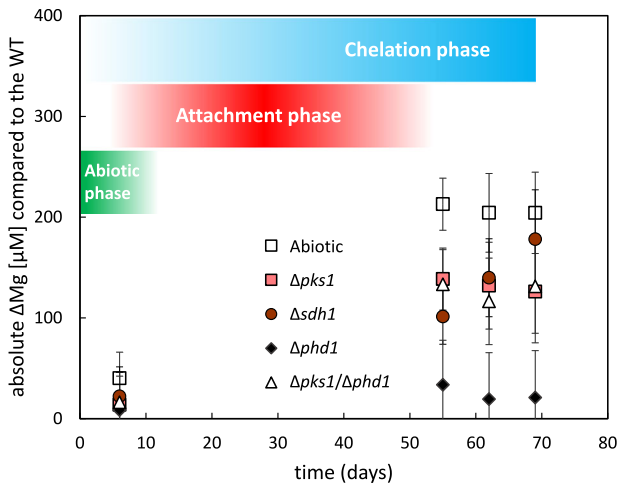

Fig. 5 The temporal evolution of the absolute difference in Mg concentration (µM) between the WT and the other set-ups using the data from Fig. 3b. Notice how this difference increased between day 6 and 55 but remained stable after day 55 for the abiotic control, and Δ*pks1* and Δ*pks1*/Δ*phd1* mutants, indicating that the effect of attachment on the dissolution of olivine in batch happened between day 6 and 55. The difference for the Δ*sdh1* mutant however kept increasing over time, indicating that the effect of the chelation of Fe lasted longer. Error bars represent twice the combined propagated uncertainties of both Mg concentrations.

using the Mg concentration difference between day 6 and 55). Inhibition of olivine dissolution was not influenced by the olivine saturation state, regardless whether mineral dissolution would obey conventional kinetics like the transition state theory[48] or unconventional kinetics like the stepwave model[49,50]. Therefore, this abiotic inhibition is likely caused by Fe oxidation (in the form of Fe(III) oxyhydroxide precipitation or in situ Fe oxidation) at the olivine surface as previously observed[51,52]. The fungus could therefore enhance olivine's dissolution in three ways: (i) by preventing this inhibition through Fe solubilisation, (ii) by cellular Fe uptake or (iii) by cellular/biofilm Fe adsorption. These Fe interaction mechanisms are positively affected by attachment to minerals. Attachment to the mineral surface could increase the production[53] and efficiency[54,55] of Fe-chelating siderophores. Both EPS[56] and melanin[57] are able to adsorb Fe. In a metal uptake experiment, biomass of the melanin-containing *K. petricola* WT had a higher Fe content compared to the biomass of the melanin-deficient Δ*pks1* mutant[58]. Close contact between olivine and these Fe sinks (i.e., melanin and EPS) might prevent Fe precipitation on the olivine surface. All these mechanisms explain the lower aqueous Fe concentration in the WT and Δ*phd1* set-ups compared to the Δ*pks1* and Δ*pks1*/Δ*phd1* set-ups (Fig. 3d): the attached, melanised cell could be able to sequestrate Fe bound by siderophores or other chelators (e.g., citrate) faster and to a higher extent, preventing them to 'leak'. By employing attachment and melanin, the WT and Δ*phd1* mutant would sequestrate Fe more efficiently than the melanin-deficient mutants, thereby increasing the olivine dissolution rate.

Another attachment-related factor of impact on the dissolution rate is the pH at the olivine-biofilm interface which could be different from the bulk pH through the local actions of the fungal metabolism. However, as shown in our previous study, the surface of olivine reacted at a pH of 3.5 is strongly etched[44], while we have never observed such strong etching patterns on the olivine surface underneath (dislodged) fungal biofilms (Supplementary Fig. 4). Thus, if the biofilm would have caused a locally acidic environment, the pH decrease was likely small. Lastly, cellular O_2 consumption could create a locally reduced environment, preventing Fe oxidation as well. All or some of the above-mentioned mechanisms could have been working in parallel.

The Δ*sdh1* mutant behaved differently from the other strains: it had the highest olivine dissolution rate but a grade of attachment not significantly different from the WT and Δ*phd1* mutant. This mutant had a protein-enriched surface (Supplementary Table 4 and Supplementary Fig. 2) and an orange-brownish colour due to the accumulation of different precursors of DHN melanin, which in contrast to melanin are partially water-soluble and thus released into the extracellular space[18], explaining the change in colour of its supernatant. As the melanin-intermediate T4HN is colourless, this orange to brown colour likely derived from its autooxidation product, flaviolin[19,59]. As phenol is able to bind a range of metal ions including Mg and Fe[60], extracellular release of such compounds may explain the higher aqueous Mg, Si, and Fe concentrations and olivine dissolution rate of this mutant (Figs. 3 and 4a). As the rate of olivine dissolution by Δ*sdh1* was unaffected by the Mg and Si concentration (neither according to the TST nor the stepwave model), an increase in the solubility of Mg or Si through the chelating abilities of secreted compounds would not affect the rate. This is different for Fe: precipitation of Fe oxides inhibits dissolution[51,52] while application of Fe-chelating siderophores enhances the dissolution rate of olivine[61]. The phenolic compounds released by the Δ*sdh1* mutant could play a role similar to siderophores, driving olivine dissolution by preventing Fe oxidation at the surface. The ever-increasing difference in the Mg concentration of the WT compared to the Δ*sdh1* mutant (Fig. 5) indicates that this chelating effect is more long-lasting in our batch conditions than the attachment effect. Apart from attaching

to olivine and solubilising Fe, this mutant also has a Fe content higher than the Δ*pks1* mutant but lower than the WT[58], showing that this incomplete melanin is still able to adsorb Fe. We hypothesise that the Δ*sdh1* mutant dissolved olivine at the highest rate due to its triple ability to attach and solubilise and adsorb Fe.

Specific mechanisms underlying fungal mineral weathering were studied with the help of genetic amendments. The importance of attachment and Fe chelation processes were shown through the characterisation of the EPS and the mineral weathering capacity of the WT and four pigment-mutants of *K. petricola*. Melanised mutants with more pullulan in the EPS matrix attached better to and dissolve olivine at a higher rate. The role of melanin synthesis intermediates is interesting: the soluble, orange-brownish compound released by the Δ*sdh1* mutant seems to have played a role similar to Fe-chelating siderophores, driving olivine dissolution even further. Extracellular matrix and substrate attachment are intrinsic properties of all biofilms and rock-inhabiting black fungi possess these features to the full extent. The specific polymeric composition of their EPS matrix -as shown using a model species *K. petricola*- facilitates substrate attachment of black fungi. When attached, the Fe sequestration and solubilisation mechanisms of fungi increase in efficiency, allowing fungi to enhance olivine's dissolution.

METHODS

Fungal strains and biofilm culture conditions

K. petricola strain A95 was isolated from a marble monument in Athens (Greece)[62]. It is maintained at the Centraalbureau voor Schimmelcultures (as CBS 123872) in Utrecht, The Netherlands, and the Federal Institute for Materials Research and Testing (as A95) in Berlin, Germany. *K. petricola* WT and pigment mutants Δ*pks1*, Δ*pks1*/Δ*phd1*, Δ*sdh1*, and Δ*phd1*[18] were cultivated in liquid malt extract broth (MEB). Subaerial biofilms produced by fungal cells were grown on cellulose acetate filters (0.45 µm; Sartorius, Göttingen, Germany) placed on malt-extract agar plates (MEA). After mechanical separation[63], 1 ml of the cell suspension was spread onto the filter and incubated at 25 °C for 7 days.

Transmission electron microscopy (TEM) and cryo-scanning electron microscopy (Cryo-SEM)

For TEM observations, mycelia from the outer, younger part of colonies were fixed using 4% glutaraldehyde (4 °C, diluted with 0.1 M phosphate buffer, pH 7.2) for 2 h. Vacuum was applied to the samples to facilitate the infiltration process. After fixation, the samples were rinsed 3 times with 0.1 M phosphate buffer and post-fixed in 2% buffered OsO_4 solution for 1 h at 4 °C. Then samples were rinsed again, dehydrated in a graded series of ethanol, and transferred into Spurr's embedding medium[64]. Ultrathin sections (70 nm) were contrasted in uranyl acetate and lead citrate according to Reynolds[65], washed, and then studied with a Philips 208 electron microscope.

Cryo-SEM of biofilms grown for seven days on cellulose acetate filters was performed using an ESEM (XL30 with wolfram cathode, Thermo Fischer Scientific/FEI Europe, Eindhoven, Netherlands) equipped with an Cryo-Transfer system (Alto 1000, Gatan, Abingdon Oxon, UK).

EPS extraction, monosaccharide composition, and linkage type determination

In general, biofilms growing on three cellulose acetate filters were scraped-off and pooled as one through suspension in 10 ml PBS buffer. EPS was extracted from these pooled samples according to Liu and Fang[66]: addition of 100 µl formaldehyde, 1 h incubation at 4 °C, addition of 4 ml 1 M NaOH, 3 h incubation at room temperature, centrifugation (7190 × *g*, 10 min), the addition of ice-cold ethanol (final 70% v/v) to supernatant, mixing, and 16 h incubation at 4 °C. To make sure that this method did not harm the cell wall or membrane, which could cause the contamination of the extract with intracellular substances, the integrity of the treated cells was checked by light microscopy. The monosaccharide units and linkage types of exopolysaccharides were analysed via their (permethylated) alditol acetates by gas chromatography-mass spectrometry as previously described[15].

The EPS amount and monosaccharide composition were based on the analysis of three or four pooled samples per biological replicate. The linkage types were based on the analysis of one pooled sample per biological replicate. For the EPS amount and linkage type, three biological replicates were analysed. For the monosaccharide composition two (or in the case of Δ*pks1*/Δ*phd1*, one) biological replicates were analysed. In the figures and text, the averages of the biological experimental replicates are given with twice the standard error of the replicates.

Fourier transform infrared (FTIR) spectroscopy

For FTIR spectroscopy, 10 µl of the extracted EPS was placed on a ZnSe-crystal (Korth Kristalle GmbH, Germany) and dried at 45 °C for 30 min. The infrared spectra were recorded with a FTIR spectrometer (Vertex 70, Bruker Optics, Germany) coupled with an infrared microscope (Hyperion 3000, Bruker Optics, Germany) using the absorbance mode in the frequency range of 4000–800 cm^{-1} with a spectral resolution of 4 cm^{-1}. All spectra were base-line corrected, the CO_2 peak was removed and represent the mean of five recorded spectra.

X-ray photoelectron spectroscopy (XPS)

The chemical composition of the EPS matrices of all strains was determined by XPS. As XPS only probes the shallowest surface layers (63% of the signal originates from less than 26 Å, and 95% from less than 78 Å[67]), we assumed that an extraction of EPS was not necessary and performed the analysis directly on freeze-dried fungal biofilms. A detailed description of the used method is given in Supplementary File, method description A. The WT and mutant strains were grown in triplicates for 9 days on Czapek-Dox solid medium (58 mM sucrose, 35 mM $NaNO_3$, 5.9 mM H_2KPO_4, 6.7 mM KCl, 4.2 mM $MgSO_4$, 0.035 mM $FeSO_4$*$7H_2O$, 15 g/l bacteriology grade agar), covered with a cellophane layer. Harvested biofilms were freeze dried (Christ, Alpha 1–4 LSCplus) overnight before XPS analysis. Due to a lack of biomass sample, the three replicates of each strain were combined and analysed twice. The measured atomic C % is likely an overestimation due to the so-called adventitious carbon[68]. We will therefore focus on the relative differences between the strains and not compare our results with previous XPS analyses of EPS. The relative analytical uncertainty within a 95% confidence interval of the atomic percentages of C, O, and N was 20% (conservative estimate). The average of the two measurements is given with the propagated uncertainty including this analytical uncertainty and twice the standard deviation of the two measurements.

Lectin screening

Primarily a binary fluorescence lectin barcoding was performed with the full-pigmented WT and the colourless mutant Δ*pks1*/Δ*phd1* as described by Neu & Kuhlicke[26] (see this reference for details regarding the lectin producers and CLSM analysis). Biofilms of both strains were grown for 7 days on MEA plates covered with cellophane sheets. For the screening small pieces (ca. 5 × 5 mm) of biofilms on cellophane were excised and placed on a microscope slide. The biofilm sample was then covered with a few droplets of fluorescently labelled lectins and incubated for 20 min at room temperature in the dark. Unbound lectins were removed by washing the sample with water and a coverslip was added. After examination of the binding of different lectins in both strains with CLSM, two lectins (i.e., HHA and GNA) were selected for a fluorescence lectin-binding analysis[26] with the WT, the Δ*pks1* mutant, and the Δ*pks1*/Δ*phd1* mutant.

Olivine dissolution experiments

Olivine dissolution experiments were carried out in batch reactors to quantify the effect of both WT and its pigment mutants on olivine dissolution. A detailed description of the procedure is given in the Supplementary File: method description B.

Mineral and reacting media

The mineral used in the batch dissolution experiments was natural forsteritic olivine (Fo90) (Hausen Mineraliengroßhandel). The crystals were crushed with an agate mortar and pestle and the 63–125 µm size fraction was separated by dry sieving. The resulting powder was ultrasonically cleaned three times using acetone and dried at 65 °C until a stable weight

was reached. The specific surface area (SSA) of the cleaned, unreacted olivine powder was measured by the BET method (ASAP2020, Micromeritics, USA) at the BAM according to DIN ISO 9277 (2014) using krypton as an adsorptive gas. Since abiotically reacted samples gave a similar (i.e., within twice the standard error) SSA as the unreacted, fresh olivine and the SSA of biotically reacted samples could not be measured (due to the presence of cells on the olivine), only the SSA of the initial fresh olivine was used to calculate the olivine dissolution rates. Electron microprobe analysis (JXA 8900-RL, JEOL) of the olivine shows a typical chemical composition for olivine [e.g., Oelkers[69],]: $Mg_{1.856\pm0.034}Fe_{0.1726\pm0.0078}SiO_4$ (mean with twice the standard deviation).

The aqueous medium used in the dissolution experiment was a minimal nutrient solution containing all essential elements except the metal(loid)s, which should be obtained by dissolving olivine. The medium (hereafter called CNPS medium) contains 298.85 µM of Na_2SO_4, 173.01 µM of K_2HPO_4*$3H_2O$, 9.95 µM of thiamine hydrochloride, 9.96 mM glucose*H_2O, 18.50 mM of NH_4NO_3 and 11.11 mM of 2-(N-morpholino)ethanesulfonic acid hydrate (MES). The pH was set at 6.00 before the medium was autoclaved. Glucose*H_2O and MES buffer were added after autoclaving using filter-sterilised stock solutions.

Fungal culturing and quantification

For inoculation of all conducted dissolution experiments, cells in their stationary growth phase were disaggregated and washed with CNPS medium. To ensure that the same amount of starter culture was used for each replicate, the cell number was quantified using a hemocytometer (Hecht-Assistent, Sondheim/Rhön, Germany), taking the average cell number from three grids.

The initial biomass was quantified as well by measuring the dry weight of the starter culture. The final biomass was estimated by subtracting the dry weight of the abiotic runs (consisting of olivine) from the dry weight of the biotic runs (consisting of olivine and biomass). The averages of the biological experimental replicates are given with once the standard error of the replicates.

Experimental set-up batch dissolution experiments

The batch dissolution experiments constituted a reactor flask with olivine powder, nutrient solution, and growing fungal biomass and was run in biological triplicates. The experiments were performed in 500 ml polycarbonate Erlenmeyer flasks with vented caps (Corning). Before autoclaving, 4 ± 0.001 g of cleaned olivine was added to each flask. After autoclaving the flasks were filled with 400 ml of CNPS medium. Biotic experiments were inoculated with a hemocytometer-quantified aliquot (i.e., 5×10^7 CFU l^{-1}) of the respective *K. petricola* culture (i. e. WT or mutant strain). The reactor flasks were incubated for 69 days in a climatic chamber (LT-36VL, Percival) under constant temperature (25 °C), constant light source (90 µmol photons m^{-2} s^{-1}), and were shaken at 150 rpm. Note that the olivine and biomass in the reactors were not in suspension because excessive shaking is not suitable for biological growth.

From the batch reactors, 5 ml samples were taken at regular time points. To keep the solid-liquid ratio constant, sampling was done whilst manually shaking the flasks, keeping all solids in suspension. Therefore, each sampling event decreased the mass of olivine in the reactor by ca. 1.25% (i.e., 5 ml sample per 400 ml total volume). These samples were filtered (0.22 µm) and either used for pH analysis, or acidified with HNO_3 (Merck, suprapure grade) to a pH < 2 and stored in acid-cleaned, polypropylene falcon tubes at 4 °C prior to dissolved element analysis by ICP-OES. At the end of the experimental runs the olivine and biomass were dried and weighed to estimate the final biomass.

Solution analysis and calculation of dissolution rates

The pH was analysed using a Blueline 25 pH electrode (Schott instruments), calibrated at pH 4, 7, and 10. The averages of the biological experimental replicates are given with either twice the analytical uncertainty of 0.01 or twice the standard error of the replicates, whichever was higher.

Concentrations of dissolved Mg, Si, and Fe were determined by ICP-OES (Varian 720-ES) analysis of the filtered and acidified solution samples in the HELGES laboratory at GFZ Potsdam, Germany[70]. For a detailed method, description see Schuessler et al.[71]. Details on this study are given in the Supplementary File, method description C. The detection limit (with once the standard deviation) was (0.1169 ± 0.0015) ppm for Mg, (0.0619 ± 0.0012) ppm for Si and (0.0055 ± 0.0002) ppm for Fe. The analytical uncertainty used to interpret the sample results is quantified based on the trueness and the precision of the repeated measurement of quality control standards (QC) and the contribution of the medium blank (i.e., the unreacted medium). The averages of the biological experimental replicates are given with either twice this analytical uncertainty or twice the standard error of the replicates, whichever was higher. For the Mg/Si and Fe/Si concentration ratios, the averages of the biological experimental replicates are given with the combined propagated uncertainties of either Mg and Si (for Mg/Si) or Fe and Si (for Fe/Si). For the absolute difference in Mg concentration between the WT and the other set-ups (i.e., $|Mg_{WT} - Mg_X|$), the averages of the biological experimental replicates are given with the combined propagated uncertainties of both Mg concentrations.

The olivine dissolution rate (r, mol cm^{-2} s^{-1}) for the batch experiments was quantified based on the temporal evolution of the concentration of accumulating released metals according to Daval et al.[72] (Eq. 1)

$$r(t) = \frac{\Delta(C_{Mg})}{\Delta t \times m_{olivine}(t) \times SSA \times \eta_{Mg}} \quad (1)$$

where $r(t)$ stands for the dissolution rate (mol cm^{-2} s^{-1}) based on the amount of Mg in solution at time t. $\Delta(C_{Mg})$ is the difference in molar amount of Mg between time t and $t-\Delta t$ (i.e., two consecutive sampling points). Δt, the time (s) between different sampling points. $m_{olivine}(t)$ is the mass (g) of olivine in the bottle just before sampling. Since the reactors were shaken strongly during sampling, we assume that the olivine was kept in suspension during sampling and therefore the mass of olivine at each sampling point was calculated by subtracting per sampling 5/400th from the initial mass (i.e., 0.05 g). SSA stands for the specific surface area of olivine at the beginning of the experiment (in cm^2 g^{-1} as measured by BET) and η_{Mg} for the stoichiometric coefficient of Mg in olivine (1.8557 as measured by electron microprobe analysis). Error bars and uncertainties reported with the average dissolution rates represent twice the combined analytical uncertainty calculated from the uncertainties of the Mg concentration difference (as measured by ICP-OES) and the SSA (as measured by the BET method) (i.e., propagated through Eq. 1) or twice the standard error of the biological replicates, whichever was higher. The uncertainty in the mass of olivine ($m_{olivine}$) and the stoichiometric coefficient of Mg (η_{Mg}) are quantified around 1% (twice the standard deviation) and are therefore non-significant compared to the uncertainties of the other analyses. The final dissolution rates shown in Fig. 4b are based on the difference between the aqueous Mg concentrations at day 6 and day 55 as the difference in Mg concentration between the samples of day 55, 62, and 69 was smaller than the analytical error of the ICP-OES analyses, causing large analytical errors and making it impossible to accurately calculate the dissolution rates after day 55.

Grade of attachment: dissecting microscope analysis

The *grade of attachment* represents the percentage of olivine grains with a rock-inhabiting fungal biofilm (i.e., colonised) and was quantified by counting the colonised olivine grains at the end of the experiment (i.e., day 69) using a dissecting microscope (Stemi 2000C, Zeiss) and dividing this number by the total number of olivine grains. Error bars and uncertainties reported with the average represent twice the standard error of the biological replicates.

Scanning electron microscope analysis

The sample preparation used in this study for SEM analysis follows Spurr[64]. Samples taken at the end of each dissolution experiment were subsequently fixed with glutaraldehyde and washed with phosphate-buffered saline (PBS). PBS was exchanged for ethanol by washing the samples with solutions with a gradual increasing ethanol concentration. The samples were then dried by critical point drying (Leica EM CPD300) and fixed onto adhesive carbon tape on a SEM sample-holder. After gold sputtering (10–15 nm), they were analysed by SEM (XL30) to observe the growth behaviour of the WT and mutants.

Thermodynamic calculations

Thermodynamic calculations were used to assess the effect of the olivine saturation state on the inhibition of olivine dissolution according to conventional and unconventional kinetics as previously done by Daval et al.[73]. The Gibbs free energy of olivine dissolution was calculated based on Eq. 2 using the thermodynamic equilibrium constant ($K_{olivine}$) from the PHREEQC database[74], and the final pH, Si, and Mg concentrations of the

respective set-up.

$$\Delta G_{\text{olivine}} = R \times T \times \ln\left(\frac{(C_{\text{Mg}})^2 \times (C_{\text{Si}})}{(C_{\text{H}^+})^4 \times K_{\text{olivine}}}\right) \quad (2)$$

Assuming that mineral dissolution would obey conventional kinetics, the following transition state theory relation according to Lasaga[48], (Eq. 3) would apply.

$$r_{\text{olivine}} = r_{\text{olivine}}^{\text{pH},T} \times \left(1 - \exp\left(\frac{\Delta G_{\text{olivine}}}{R \times T}\right)\right) \quad (3)$$

As $r_{\text{olivine}}^{\text{pH},T}$ is the dissolution rate far from equilibrium, a $\frac{r_{\text{olivine}}}{r_{\text{olivine}}^{\text{pH},T}}$ of 1 would imply that inhibition of dissolution due to the approach of equilibrium is absent. However, dissolution could also obey unconventional kinetic models like the stepwave model[48,49]. This model implies that dissolution is controlled by etch pit nucleation, which is spontaneous as long as the Gibbs free energy of olivine dissolution remains below the critical Gibbs free energy of etch pit nucleation (which has a minimal expected value of −12.0 kJ/mol[73]).

Statistics

To assess the differences in the means among the strains for the measured variables, we assumed a normal distribution and used one-way analysis of variance (ANOVA) with Tukey-HSD post hoc test using Origin 2020 statistical software. We also quantified the 95% or 99% confidence intervals.

Moreover, Pearson's correlation test was conducted for the EPS amount, pullulan-related Glcp linkages, grade of attachment at day 69, and dissolution rate at day 55 ($n = 5$). A mean value was calculated from three replicates of each strain for each variable. We did not apply any p-value correction due to the low sample size, although we are aware of increases in the type I error rate. We used correlation package (v0.7.0;) in R software (v4.0.2;).

DATA AVAILABILITY

The data generated during this study and supporting the findings of this study will be made available on the Publica website from the BAM (https://opus4.kobv.de/opus4-bam/home), under the title of this study. The strains generated for this study are available upon request.

Received: 16 November 2021; Accepted: 6 May 2022;
Published online: 26 May 2022

REFERENCES

1. Gadd, G. M. Geomycology: Fungi as agents of biogeochemical change. *Biol. Environ.: Proc. R. Ir. Acad.* **113B**, 139–153 (2018).
2. Drake, H. et al. Anaerobic consortia of fungi and sulfate reducing bacteria in deep granite fractures. *Nat. Commun.* https://doi.org/10.1038/s41467-017-00094-6 (2017).
3. Gadd, G. M. Geomycology: Biogeochemical transformations of rocks, minerals, metals and radionuclides by fungi, bioweathering and bioremediation. *Mycol. Res.* **111**, 3–49 (2007).
4. Gorbushina, A. A., Beck, A. & Schulte, A. Microcolonial rock inhabiting fungi and lichen photobionts: Evidence for mutualistic interactions. *Mycol. Res.* **109**, 1288–1296 (2005).
5. Kendrick, B. *Fungi: Ecological Importance and Impact on Humans* (eLS, 2011).
6. Naranjo-Ortiz, M. A. & Gabaldón, T. Fungal evolution: major ecological adaptations and evolutionary transitions. *Biol. Rev.* **94**, 1443–1476 (2019).
7. Flemming, H. C. *The Perfect Slime* (IWA Publishing, 2017).
8. Gueidan, C. et al. A rock-inhabiting ancestor for mutualistic and pathogen-rich fungal lineages. *Stud. Mycol.* **61**, 111–119 (2008).
9. Selbmann, L. et al. Shed light in the daRk lineagES of the fungal tree of life—STRES. *Life* **10**, 362 (2020).
10. Gorbushina, A. A. Life on the rocks. *Environ. Microbiol.* **9**, 1613–1631 (2007).
11. Mergelov, N. et al. Alteration of rocks by endolithic organisms is one of the pathways for the beginning of soils on Earth. *Sci. Rep.* **8**, 3367 (2018).
12. Noack-Schönmann, S. et al. Sub-aerial biofilms as blockers of solar radiation: Spectral properties as tools to characterise material-relevant microbial growth. *Int. Biodeter. Biodegr.* **86**, 286–293 (2014).
13. Knabe, N. & Gorbushina, A. *Methods in Microbiology* Vol. 45 (Academic Press, 2018).
14. Gerrits, R. et al. High-resolution imaging of fungal biofilm-induced olivine weathering. *Chem. Geol.* **559**, 119902 (2021).
15. Breitenbach, R. et al. Corrosive extracellular polysaccharides of the rock-inhabiting model fungus Knufia petricola. *Extremophiles* **22**, 165–175 (2018).
16. Gorbushina, A. A. et al. Black fungal colonies as units of survival: Hyphal mycosporines synthesized by rock-dwelling microcolonial fungi. *Can. J. Bot.* **81**, 131–138 (2003).
17. Butler, M. J. & Day, A. W. Fungal melanins: A review. *Can. J. Microbiol.* **44**, 1115–1136 (1998).
18. Voigt, O. et al. An advanced genetic toolkit for exploring the biology of the rock-inhabiting black fungus Knufia petricola. *Sci. Rep.* **10**, 22021 (2020).
19. Schumacher, J. DHN melanin biosynthesis in the plant pathogenic fungus Botrytis cinerea is based on two developmentally regulated key enzyme (PKS)-encoding genes. *Mol. Microbiol.* **99**, 729–748 (2016).
20. Rosas, A. L. & Casadevall, A. Melanization affects susceptibility of Cryptococcus neoformans to heat and cold. *FEMS Microbiol. Lett.* **153**, 265–272 (1997).
21. Robinson, C. H. Cold adaptation in Arctic and Antarctic fungi. *N. Phytol.* **151**, 341–353 (2001).
22. Fogarty, R. V. & Tobin, J. M. Fungal melanins and their interactions with metals. *Enzym. Micro. Tech.* **19**, 311–317 (1996).
23. Fernandez, C. W. & Koide, R. T. The function of melanin in the ectomycorrhizal fungus Cenococcum geophilum under water stress. *Fungal Ecol.* **6**, 479–486 (2013).
24. Kejzar, A., Gobec, S., Plemenitas, A. & Lenassi, M. Melanin is crucial for growth of the black yeast Hortaea werneckii in its natural hypersaline environment. *Fungal Biol.* **117**, 368–379 (2013).
25. Welch, S. A. & Vandevivere, P. Effect of microbial and other naturally occurring polymers on mineral dissolution. *Geomicrobiol. J.* **12**, 227–238 (1994).
26. Neu, T. R. & Kuhlicke, U. Fluorescence lectin bar-coding of glycoconjugates in the extracellular matrix of biofilm and bioaggregate forming microorganisms. *Microorganisms* https://doi.org/10.3390/microorganisms5010005 (2017).
27. Williams, D. H. & Fleming, I. *Spectroscopic Methods in Organic Chemistry* 4 edn (McGRAW-HILL Book Company (UK) Limited, 1989).
28. Kacurakova, M., Capek, P., Sasinkova, V., Wellner, N. & Ebringerova, A. FT-IR study of plant cell wall model compounds: pectic polysaccharides and hemicelluloses. *Carbohydr. Polym.* **43**, 195–203 (2000).
29. Cerna, M. et al. Use of FT-IR spectroscopy as a tool for the analysis of polysaccharide food additives. *Carbohydr. Polym.* **51**, 383–389 (2003).
30. Flemming, H. C. et al. Biofilms: An emergent form of bacterial life. *Nat. Rev. Microbiol.* **14**, 563–575 (2016).
31. Chan, K.-Y., Xu, L.-C. & Fang, H. H. P. Anaerobic electrochemical corrosion of mild steel in the presence of extracellular polymeric substances produced by a culture enriched in sulfate-reducing bacteria. *Environ. Sci. Technol.* **36**, 1720–1727 (2002).
32. Mahapatra, S. & Banerjee, D. Fungal exopolysaccharide: Production, composition, and applications. *Microbiol. Insights* **6**, 1–16 (2013).
33. Sterflinger, K. & Krumbein, W. E. Dematiaceous fungi as a major agent for biopitting on Mediterranean marbles and limestones. *Geomicrobiol. J.* **14**, 219–230 (1997).
34. Latge, J. P. et al. Chemical and immunological characterization of the extracellular galactomannan of Aspergillus-Fumigatus. *Infect. Immun.* **62**, 5424–5433 (1994).
35. Sassaki, G. L. et al. Some biomolecules and a partially O-acetylated exo-galactomannan containing beta-Galf units from pathogenic Exophiala jeanselmei, having a pronounced immunogenic response. *Int. J. Biol. Macromol.* **48**, 177–182 (2011).
36. Shibata, N. & Okawa, Y. Chemical structure of beta-galactofuranose-containing polysaccharide and O-linked oligosaccharides obtained from the cell wall of pathogenic dematiaceous fungus Fonsecaea pedrosoi. *Glycobiology* **21**, 69–81 (2011).
37. Henry, C. et al. Two KTR mannosyltransferases are responsible for the biosynthesis of cell wall mannans and control polarized growth in Aspergillus fumigatus. *Mbio.* https://doi.org/10.1128/mBio.02647-18 (2019).
38. Damveld, R. A. et al. A novel screening method for cell wall mutants in Aspergillus niger identifies UDP-galactopyranose mutase as an important protein in fungal cell wall biosynthesis. *Genetics* **178**, 873–881 (2008).
39. Lamarre, C. et al. Galactofuranose attenuates cellular adhesion of Aspergillus fumigatus. *Cell Microbiol.* **11**, 1612–1623 (2009).
40. El-Ganiny, A. M., Sheoran, I., Sanders, D. A. R. & Kaminskyj, S. G. W. Aspergillus nidulans UDP-glucose-4-epimerase UgeA has multiple roles in wall architecture, hyphal morphogenesis, and asexual development. *Fungal Genet. Biol.* **47**, 629–635 (2010).
41. Paul, B. C., El-Ganiny, A. E., Abbas, M., Kaminskyj, S. G. W. & Dahms, T. E. S. The role of -galactofuranose in cell wall surface structure and elasticity of Aspergillus Nidulans. *Biophys. J.* **100**, 163–163 (2011).
42. Cordero, R. J. B. & Casadevall, A. Functions of fungal melanin beyond virulence. *Fungal Biol. Rev.* **31**, 99–112 (2017).
43. Zhong, J. Y., Frases, S., Wang, H., Casadevall, A. & Stark, R. E. Following fungal melanin biosynthesis with solid-state NMR: Biopolyrner molecular structures and possible connections to cell-wall polysaccharides. *Biochemistry* **47**, 4701–4710 (2008).
44. Gerrits, R. et al. How the rock-inhabiting fungus K. petricola A95 enhances olivine dissolution through attachment. *Geochim. Cosmochim. Acta* **282**, 76–97 (2020).

45. Bardage, S. L. & Bjurman, J. Isolation of an Aureobasidium pullulans polysaccharide that promotes adhesion of blastospores to water-borne paints. *Can. J. Microbiol.* **44**, 954–958 (1998).
46. Pouliot, J. M., Walton, I., Parkhouse, M. N., Abu-Lail, L. I. & Camesano, T. A. Adhesion of *Aureobasidium pullulans* is controlled by uronic acid based polymers and pullulan. *Biomacromolecules* **6**, 1122–1131 (2005).
47. Rimstidt, J. D., Brantley, S. L. & Olsen, A. A. Systematic review of forsterite dissolution rate data. *Geochim. Cosmochim. Acta* **99**, 159–178 (2012).
48. Lasaga, A. C. *Kinetics of Geochemical Processes* (De Gruyter, 1981).
49. Lasaga, A. C. & Blum, A. E. Surface chemistry, etch pits and mineral-water reactions. *Geochim. Cosmochim. Acta* **50**, 2363–2379 (1986).
50. Lasaga, A. C. & Luttge, A. Variation of crystal dissolution rate based on a dissolution stepwave model. *Science* **291**, 2400–2404 (2001).
51. Santelli, C. M., Welch, S. A., Westrich, H. R. & Banfield, J. F. The effect of Fe-oxidizing bacteria on Fe-silicate mineral dissolution. *Chem. Geol.* **180**, 99–115 (2001).
52. Saldi, G. D. et al. Mineralogical evolution of Fe-Si-rich layers at the olivine-water interface during carbonation reactions. *Am. Miner.* **100**, 2655–2669 (2015).
53. Ahmed, E. & Holmstrom, S. J. M. Microbe-mineral interactions: The impact of surface attachment on mineral weathering and element selectivity by microorganisms. *Chem. Geol.* **403**, 13–23 (2015).
54. Völker, C. & Wolf-Gladrow, D. A. Physical limits on iron uptake mediated by siderophores or surface reductases. *Mar. Chem.* **65**, 227–244 (1999).
55. Rizzi, A., Roy, S., Bellenger, J. P. & Beauregard, P. B. Iron homeostasis in Bacillus subtilis requires siderophore production and biofilm formation. *Appl. Environ. Microb.* https://doi.org/10.1128/AEM.02439-18 (2019).
56. Tapia, J. M., Muñoz, J. A., González, F., Blázquez, M. L. & Ballester, A. Mechanism of adsorption of ferric iron by extracellular polymeric substances (EPS) from a bacterium Acidiphilium sp. *Water Sci. Technol.* **64**, 1716–1722 (2011).
57. Jacobson, E. S., Hove, E. & Emery, H. S. Antioxidant function of melanin in black fungi. *Infect. Immun.* **63**, 4944–4945 (1995).
58. Gerrits, R. *An Experimental Study of Fungal Olivine Weathering* (Freie Universität Berlin, 2019).
59. Tokousbalides, M. C. & Sisler, H. D. Site of inhibition by tricyclazole in the melanin biosynthetic pathway of Verticillium dahliae. *Pestic. Biochem. Phys.* **11**, 64–73 (1979).
60. Dunbar, R. C. Metal cation binding to phenol: DFT comparison of the competing sites. *J. Phys. Chem.* **106**, 7328–7337 (2002).
61. Torres, M. A., Dong, S., Nealson, K. H. & West, A. J. The kinetics of siderophore-mediated olivine dissolution. *Geobiology* **17**, 401–416 (2019).
62. Gorbushina, A. A., Kotlova, E. R. & Sherstneva, O. A. Cellular responses of microcolonial rock fungi to long-term desiccation and subsequent rehydration. *Stud. Mycol.* **61**, 91–97 (2008).
63. Nai, C. et al. Nutritional physiology of a rock-inhabiting, model microcolonial fungus from an ancestral lineage of the Chaetothyriales (Ascomycetes). *Fungal Genet. Biol.* **56**, 54–66 (2013).
64. Spurr, A. R. A low-viscosity epoxy resin embedding medium for electron microscopy. *J. Ultrastruct. Res.* **26**, 31–43 (1969).
65. Reynolds, E. S. The use of lead citrate at high Ph as an electron-opaque stain in electron-microscopy. *J. Cell Biol.* **17**, 208–212 (1963).
66. Liu, H. & Fang, H. H. Extraction of extracellular polymeric substances (EPS) of sludges. *J. Biotechnol.* **95**, 249–256 (2002).
67. Hochella, M. F. & Carim, A. H. A reassessment of electron-escape depths in silicon and thermally grown silicon dioxide thin-films. *Surf. Sci.* **197**, 260–268 (1988).
68. Miller, D. J., Biesinger, M. C. & McIntyre, N. S. Interactions of CO2 and CO at fractional atmosphere pressures with iron and iron oxide surfaces: one possible mechanism for surface contamination? *Surf. Interface Anal.* **33**, 299–305 (2002).
69. Oelkers, E. H. An experimental study of forsterite dissolution rates as a function of temperature and aqueous Mg and Si concentrations. *Chem. Geol.* **175**, 485–494 (2001).
70. von Blanckenburg, F., Wittmann, H., Schuessler, J. A. HELGES: Helmholtz Laboratory for the Geochemistry of the Earth Surface. *J. Large-Scale Res. Facilities* https://doi.org/10.17815/jlsrf-2-141 (2016).
71. Schuessler, J. A., Kampf, H., Koch, U. & Alawi, M. Earthquake impact on iron isotope signatures recorded in mineral spring water. *J. Geophys. Res.-Sol. Ea.* **121**, 8548–8568 (2016).
72. Daval, D. et al. Influence of amorphous silica layer formation on the dissolution rate of olivine at 90 °C and elevated pCO(2). *Chem. Geol.* **284**, 193–209 (2011).
73. Daval, D., Choblet, G., Sotin, C. & Guyot, F. Theoretical considerations on the characteristic timescales of hydrogen generation by serpentinization reactions on enceladus. *J. Geophys. Res.: Planets* https://doi.org/10.1029/2021JE006995 (2022).
74. Parkhurst, D. L. *User's Guide to PHREEQC: A Computer Program for Speciation, Reaction-Path, Advective-Transport, and Inverse Geochemical Calculations*. (U.S. Geological Survey, 1995).

ACKNOWLEDGEMENTS

We would like to thank Oliver Voigt for helping with the generation of the knock-out mutants, Evgenia Bajer for the electron microprobe analysis, and Annett Zimathies and Carsten Prinz for the BET analysis. Jörg Toepel is thanked for his help with the FTIR analysis and Ute Schoknecht and Helena Mathies are thanked for their help regarding the GC analyses. We are grateful for the help of Thomas Neu and Ute Kuhlicke regarding the lectin screening. Renate Radek and Christoph Böttcher specifically and the BioSupraMol centre in general are thanked for their help with the TEM analyses. Lastly, we are grateful to be able to do ICP-OES analyses in the HELGES laboratory at GFZ, Potsdam. This study was funded by internal funds of the BAM.

AUTHOR CONTRIBUTIONS

R.B. planned and performed the EPS quantification, glycosidic analyses, linkage analyses, CLSM analyses of the lectins, and TEM analyses. R.G. planned and performed the olivine dissolution experiments and ICP-OES analysis and planned the XPS analyses. P.D. adapted TEM protocols for *K. petricola*, planned and performed the TEM analyses. N.K. planned and performed the TEM and CLSM analyses, generated the gene deletion mutants, and supervised the project. J.R. performed the XPS analyses. I.F. performed the SEM and cryo-SEM analyses. M.R. performed statistical correlation analyses. J.S. supervised the project. A.A.G. performed the cryo-SEM analysis, supervised the project, networking, and acquired funding. The first draft of the manuscript was written by R.G., R.B., and A.A.G. All authors contributed to the final version of the manuscript. R.B. and R.G. contributed equally to this study and are considered co-first authors.

FUNDING

Open Access funding enabled and organized by Projekt DEAL.

COMPETING INTERESTS

The authors declare no competing interests.

ADDITIONAL INFORMATION

Supplementary information The online version contains supplementary material available at https://doi.org/10.1038/s41529-022-00253-1.

Correspondence and requests for materials should be addressed to Anna A. Gorbushina.

Reprints and permission information is available at http://www.nature.com/reprints

Publisher's note Springer Nature remains neutral with regard to jurisdictional claims in published maps and institutional affiliations.